

Influence of textural statistics on drag reduction by scalable, randomly rough superhydrophobic surfaces in turbulent flow ^{EP}

Cite as: Phys. Fluids **31**, 042107 (2019); <https://doi.org/10.1063/1.5090514>

Submitted: 28 January 2019 . Accepted: 24 March 2019 . Published Online: 22 April 2019

Anoop Rajappan ^{id}, Kevin Golovin ^{id}, Brian Tobelmann, Venkata Pillutla, Abhijeet, Wonjae Choi (최원재), Anish Tuteja ^{id}, and Gareth H. McKinley ^{id}

COLLECTIONS

^{EP} This paper was selected as an Editor's Pick



View Online



Export Citation



CrossMark

ARTICLES YOU MAY BE INTERESTED IN

[Geometric optimization of riblet-textured surfaces for drag reduction in laminar boundary layer flows](#)

Physics of Fluids **31**, 053601 (2019); <https://doi.org/10.1063/1.5090881>

[The formation mechanism of recirculating wake for steady flow through and around arrays of cylinders](#)

Physics of Fluids **31**, 043607 (2019); <https://doi.org/10.1063/1.5090817>

[Deviation from capillary number scaling of nonlinear viscous fingering formed by the injection of Newtonian surfactant solution](#)

Physics of Fluids **31**, 042108 (2019); <https://doi.org/10.1063/1.5090827>

CAPTURE WHAT'S POSSIBLE
WITH OUR NEW PUBLISHING ACADEMY RESOURCES

Learn more

AIP Publishing

Influence of textural statistics on drag reduction by scalable, randomly rough superhydrophobic surfaces in turbulent flow

Cite as: *Phys. Fluids* **31**, 042107 (2019); doi: [10.1063/1.5090514](https://doi.org/10.1063/1.5090514)

Submitted: 28 January 2019 • Accepted: 24 March 2019 •

Published Online: 22 April 2019



Anoop Rajappan,¹  Kevin Golovin,²  Brian Tobelmann,² Venkata Pillutla,³ Abhijeet,³ Wonjae Choi (최원재),^{3,4} Anish Tuteja,^{2,5,6}  and Gareth H. McKinley¹ 

AFFILIATIONS

¹Department of Mechanical Engineering, Massachusetts Institute of Technology, Cambridge, Massachusetts 02139, USA

²Department of Materials Science and Engineering, University of Michigan, Ann Arbor, Michigan 48109, USA

³Department of Mechanical Engineering, University of Texas at Dallas, Richardson, Texas 75080, USA

⁴Gildart Haase School of Computer Sciences and Engineering, Fairleigh Dickinson University, Teaneck, New Jersey 07666, USA

⁵Department of Chemical Engineering, University of Michigan, Ann Arbor, Michigan 48109, USA

⁶Biointerfaces Institute, University of Michigan, Ann Arbor, Michigan 48109, USA

ABSTRACT

We investigate the influence of statistical measures of surface roughness on the turbulent drag reduction (DR) performance of four scalable, randomly rough superhydrophobic (SH) textures. Each surface was fabricated using readily scalable surface texturing processes to generate a random, self-affine height profile on the base substrate. The frictional drag on all four SH surfaces was measured when fully submerged in shear-driven turbulent flow inside a bespoke Taylor-Couette apparatus at Reynolds numbers in the range $1 \times 10^4 \lesssim \text{Re} \lesssim 1 \times 10^5$. An “effective” slip length quantifying the overall drag-reducing ability for each surface was extracted from the resulting Prandtl-von Kármán friction plots. Reductions in the frictional drag of up to 26% were observed, with one of the hierarchically textured surfaces exceeding a wall shear stress of 26 Pa (corresponding to a Reynolds number $\text{Re} \approx 7 \times 10^4$) before the onset of flow-induced plastron collapse. The surface morphology of each texture was characterized using noncontact optical profilometry, and the influence of various statistical measures of roughness on the effective slip length was explored. The lateral autocorrelation length was identified as the key textural parameter determining the drag-reducing ability for randomly rough SH textures, playing the role analogous to the spatial periodicity of regularly patterned SH surfaces. A large autocorrelation length, a small surface roughness, and the presence of hierarchical roughness features were observed to be the three important design requirements for scalable SH textures for optimal DR in turbulent flows.

Published under license by AIP Publishing. <https://doi.org/10.1063/1.5090514>

I. INTRODUCTION

Skin friction accounts for a significant fraction of the total hydrodynamic resistance on surface and subsurface watercraft; under normal service conditions, approximately 50% of the total drag on ships and 60% of the drag on submarines arise from frictional shear stresses on the hull.¹ It is estimated that approximately 60% of the propulsive power of a typical displacement ship is expended in overcoming viscous resistance.² Techniques to reduce skin friction, even moderately, can therefore produce substantial savings in fuel consumption and operating costs through

improvements in ship speed and efficiency. The development of successful drag reduction (DR) strategies thus has potential economic, strategic, and environmental benefits.

Several active and passive methods of reducing skin friction have been explored in the past, with varying levels of success.¹ Active methods for frictional drag reduction include injection of air bubbles³ or high molecular weight polymers⁴ into the turbulent boundary layer as well as incorporating submerged air-filled recesses under the hull.⁵ These methods require some form of continuous input to sustain drag reduction and become economically viable in long-haul operations only if the costs involved in active flow modification

are offset by the savings in fuel and operating costs.¹ Passive drag reduction methods, on the other hand, do not require any form of continuous energy input but usually produce a smaller percentage reduction in drag than active methods. For example, shark-skin inspired riblet surfaces have been extensively investigated in the literature and are reported to reduce the wall shear stress in turbulent boundary layer flows by modifying the near-wall vortex dynamics.⁶ Recently, the application of superhydrophobic (SH) coatings to the hull has gained interest as a potential technique for skin friction reduction on ships and undersea vehicles.^{1,7,8} However, scalable SH surfaces that can successfully operate at high Reynolds numbers ($10^8 \leq \text{Re} \leq 10^9$) typically encountered in marine applications are yet to be developed.⁷

Superhydrophobic textures are characterized by large apparent contact angles (greater than 150°) and very low contact angle hysteresis (typically less than 5°); a water meniscus spreading laterally over the SH surface simply bridges across surface asperities, leaving pockets of air confined between the solid substrate and the newly formed air-water interface.⁹ This results in a composite wetting configuration called the Cassie-Baxter state, in which a large areal fraction of the underlying solid is separated from the liquid phase by the intervening air layer. When submerged underwater, this layer of air, also called a plastron,¹⁰ can remain trapped between the texture asperities, inducing slip and reducing the frictional shear stress in wall-bounded flows.¹¹ Examples of similar drag reduction strategies can also be found in nature; emperor penguins, for instance, are known to successfully utilize the air trapped within their water repellent feathers to reduce drag as they resurface from dives.¹²

Flow over a submerged SH wall in the Cassie-Baxter state encounters intermittent regions of direct contact with the solid substrate, interspersed between large areas where the flow is separated from the wall by the air layer trapped in the texture. Whereas the usual no-slip condition applies in the regions of solid-liquid contact, the liquid-air interfaces bridging the asperities of the texture act effectively as shear-free boundaries since the viscosity of air is considerably smaller than that of water (by a factor of almost 50 at room temperature). Consequently, the flow partially slips over the texture, and the net shear stress on the wall is reduced because of the diminished contact between the solid substrate and the flow.¹¹ The heterogeneous boundary condition over a superhydrophobic texture is often modeled by prescribing an equivalent slip velocity $\mathbf{v} = (U_s, V_s)$ at the wall, given by the Navier slip condition¹³

$$U_s = b_x \left. \frac{\tau_{zx}}{\mu} \right|_{z=0} \quad \text{and} \quad V_s = b_y \left. \frac{\tau_{zy}}{\mu} \right|_{z=0}. \quad (1)$$

Here x , y , and z are, respectively, the streamwise, spanwise, and wall-normal coordinates; τ_{zx} and τ_{zy} are components of the shear stress acting on the wall (with the mean plane located at $z = 0$); b_x and b_y are the streamwise and spanwise slip lengths on the surface; and μ is the dynamic viscosity of the liquid phase. On a randomly generated SH texture, we expect the slip to be isotropic, giving a single characteristic slip length $b = b_x = b_y$. Analytical expressions for the effective slip length in the Stokes flow over periodic arrays of longitudinal and transverse shear-free slots were first derived by Philip;^{14,15} results for other similar flow configurations were subsequently derived by Lauga and Stone,¹⁶ Cottin-Bizonne *et al.*,¹⁷ and Schönecker *et al.*¹⁸ Generic scaling laws for the slip length on

superhydrophobic surfaces in the creeping flow limit were obtained by Ybert *et al.*¹⁹ who showed that as the areal fraction ϕ of the surface wetted by the flow approaches zero, the slip length b on a superhydrophobic texture patterned with a two-dimensional array of micro-posts scales as $b \sim L/\sqrt{\phi}$, where L is the spatial periodicity of the post pattern.

Superhydrophobic drag reduction in turbulent flow brings several new challenges not present in the laminar case.⁷ Large velocity and pressure fluctuations in strongly turbulent flow can trigger a wetting transition to the Wenzel state,²⁰ after which the surface texture simply acts as hydrodynamic roughness, increasing frictional drag. The viscous sublayer and near wall coherent structures can interact in complex ways with the roughness elements of the texture and potentially offset any friction reduction arising from wall slip. Min and Kim²¹ performed direct numerical simulation (DNS) studies of turbulent channel flow with prescribed streamwise or spanwise slip boundary conditions at the wall; they showed that even as streamwise slip resulted in drag reduction, spanwise slip led to strengthening of near wall vortex structures, enhancing turbulent momentum transport and increasing the frictional shear stress on the wall. This mechanism of drag increase is unique to turbulent flows and is wholly absent in laminar flows. On random textures which have equal slip lengths in both streamwise and spanwise directions, drag reduction generated by streamwise slip is therefore partly offset by the drag increase due to spanwise slip. Martell *et al.*²² arrived at similar conclusions regarding the effect of streamwise and spanwise slip and in a separate study showed that drag reduction in turbulent flow increases with the Reynolds number, in contrast to the case of laminar flow.²³ More recently, Seo and Mani²⁴ derived a scaling law for the evolution of the slip length on SH textures in the high Reynolds number limit and validated it using DNS results. In their analysis, a laminar boundary layer is assumed to develop over each solid-liquid contact spot, and the resulting scaling law for slip length is given by $b^+ \sim (L^+)^{1/3} \phi^{-1/2}$, where L^+ and b^+ are, respectively, the surface periodicity and the slip length scaled by the near-wall viscous length scale $\delta_v = \sqrt{\rho\nu^2/\tau_w}$, where ρ and ν denote the density and kinematic viscosity of the liquid phase, respectively, and τ_w is the average shear stress at the wall. Unlike the result for low Reynolds numbers, the dimensional slip length $b \sim L^{1/3} \delta_v^{2/3} \phi^{-1/2}$ is now also a weakly decreasing function of the wall shear stress τ_w because this stress determines the characteristic length scale δ_v .

Practical drag reduction applications require scalable SH textures that can be easily applied over large areas of the solid boundary in contact with the flow;^{1,7} for instance, the wet hull area of ships and submarines can be of the order of $\sim 100\text{--}1000 \text{ m}^2$. On smaller scales, regularly patterned superhydrophobic surfaces consisting of periodic arrays of ridges or posts have been extensively investigated for antiwetting and drag reduction applications over the past two decades. For example, several studies in the literature have reported careful experimental measurements of turbulent drag reduction by SH textures comprising periodically spaced microgrooves aligned in the flow direction.^{25–27} As noted above, accurate scaling laws governing slip length over these “canonical” textures are well known from previous theoretical and computational studies in the literature.^{19,24} However, fabrication of these surfaces often requires expensive and precise manufacturing techniques, which limits their scalability to real-life applications.

Randomly rough SH surfaces, on the other hand, can be produced by relatively inexpensive and easily scalable techniques, such as spray-coating, sandblasting, and chemical or electrochemical etching, which are already in widespread use in industrial-scale surface treatment processes. Samaha *et al.*²⁸ prepared randomly rough SH surfaces by depositing hydrophobic aerogel silica beads on a metal substrate and measured the slip length and percentage drag reduction in laminar flow using a parallel-plate rheometer. Moaven *et al.*²⁹ produced scalable SH textures by spray-coating a sandblasted aluminum substrate with titania nanoparticles and performed flow measurements using a rotating disk apparatus; drag reduction up to 15% was reported under turbulent flow conditions, corresponding to speeds of 8–12 m s⁻¹ and Reynolds numbers $Re \approx 5 \times 10^5 - 8 \times 10^5$ at the rim.

Unlike regularly patterned surfaces, the morphology of randomly rough SH surfaces is generally more difficult to characterize, and a scaling law for slip length in terms of surface roughness parameters is yet to be derived. Whereas a large number of randomly rough surfaces have shown extraordinary success in antiwetting applications,^{30,31} most of them do not perform equally well in drag reduction; indeed, many strongly water-repellent SH surfaces are found to produce no drag reduction in turbulent flow, even when they remain perfectly nonwet underwater.⁷ This underlines the necessity of investigating in detail the particular textural features of the surface profile which confer the ability to reduce drag under turbulent flow conditions. In contrast to regularly patterned textures, the available experimental data for turbulent drag reduction on random textures have sometimes been inconclusive or even contradictory; drag reduction and drag increase have both been reported on similar surface textures.^{7,32–34} The disparities in experimental results may also arise from differences in surface preparation and flow conditions, which vary between test facilities. Unlike the case of regular arrays of ridges and posts for which the wetting transition is abrupt, the liquid-air interface on a random texture traverses several intermediate metastable configurations with increasing external pressure;³⁵ plastron collapse thus occurs progressively and may not be immediately apparent. As the air-water interface penetrates deeper into the texture, the wetted solid fraction increases, altering the effective slip length; consequently, identical rough textures tested under different flow conditions can yield significantly different values of slip length.

A number of recent studies have focused on addressing this gap in understanding of the relationship between surface morphology of rough SH surfaces and their drag-reducing ability in turbulent flow. From experimental measurements, Bidkar *et al.*³⁶ concluded that in addition to retaining a Cassie-Baxter state when submerged, the texture must also possess a low surface roughness to produce a net reduction in drag; specifically, the roughness of the surface had to be small in comparison to the viscous length scale of the turbulent boundary layer. Gose *et al.*³⁷ performed skin friction measurements on four randomly rough superhydrophobic textures using a channel flow facility at Reynolds numbers in the range $1 \times 10^4 \leq Re \leq 3 \times 10^4$ and wall shear stresses up to 65 Pa. They reported that a net positive drag reduction was observed only when the product of the surface roughness (scaled in wall units) and the contact angle hysteresis of a sessile drop on the surface measured at small drop volumes (i.e., at high internal Laplace pressures) was minimized.

In this study, we evaluate the drag-reducing ability of four randomly rough superhydrophobic surfaces in turbulent flow and attempt to correlate this with statistical measures of the roughness profile. All test surfaces were produced by readily scalable mechanical or chemical texturing processes, such as sand blasting, chemical etching, boehmitization,³⁸ and spray coating. A custom-built Taylor-Couette (TC) fixture was used to perform skin friction measurements on the surfaces under fully developed turbulent flow conditions. Flow tests over a range of Reynolds numbers, in conjunction with surface profile measurements, are used to investigate the influence of specific measures of surface roughness on the particular traits desirable in turbulent drag reduction applications, namely, large slip lengths and excellent resistance to pressure-induced wetting.

II. FABRICATION OF SCALABLE SUPERHYDROPHOBIC SURFACES

The four prototype drag-reducing surfaces used in this study were an acrylic-based fluorinated polyhedral oligomeric silsesquioxane (FPOSS) spray-on coating, a chemically etched aluminum surface, and two different sandblasted, etched, and boehmitized aluminum textures. Their fabrication is briefly described below.

A. Acrylic FPOSS spray-on coating

This surface was fabricated by spray-coating a clean aluminum surface with a mixture of a high molecular weight polymer binder and a low surface energy hydrophobizing agent, following Srinivasan *et al.*^{8,39} The spray solution was prepared by dissolving 25 g l⁻¹ of poly(methyl methacrylate) of molecular weight 75 kDa (Scientific Polymer Products, Inc.) and 25 g l⁻¹ of 1H,1H,2H,2H-tridecafluorooctyl polyhedral oligomeric silsesquioxane or “FPOSS” (NBD Nanotechnologies, Inc.) in the volatile fluorinated solvent AK-225 (Asahi Glass Company). The solution was sprayed uniformly over the smooth aluminum substrate using a hand-held airbrush (0.3 mm nozzle diameter) and allowed to dry in ambient air at room temperature for 3 h. The polymer matrix deposited on the surface had a corpuscular microstructure³⁹ with roughness features approximately 10 μm–50 μm in size, as seen in Fig. 1(a).

B. Etched aluminum

This surface was prepared using a subtractive acid-etching process, based on the surface modification technique previously reported by Yang *et al.*⁴⁰ The aluminum 6061-T6 substrate was first cleaned thoroughly and then immersed in 2.5M aqueous hydrochloric acid for 20 min to generate the rough microtexture. After cleaning off the etching residue by sonication, the surface was boehmitized in boiling deionized water for 20 min, during which the native oxide layer dissolves and redeposits as a conformal layer of boehmite crystals, conferring an additional level of nanoscale roughness above and beyond that produced by etching.³⁸ Finally, the textured surface was hydrophobized by vapor phase deposition of 1H,1H,2H,2H-heptadecafluorodecyl triethoxysilane at 80 °C under vacuum. Figure 1(b) shows a depth-composed optical micrograph of the final surface, and the microscale roughness produced by the etching process is clearly visible.

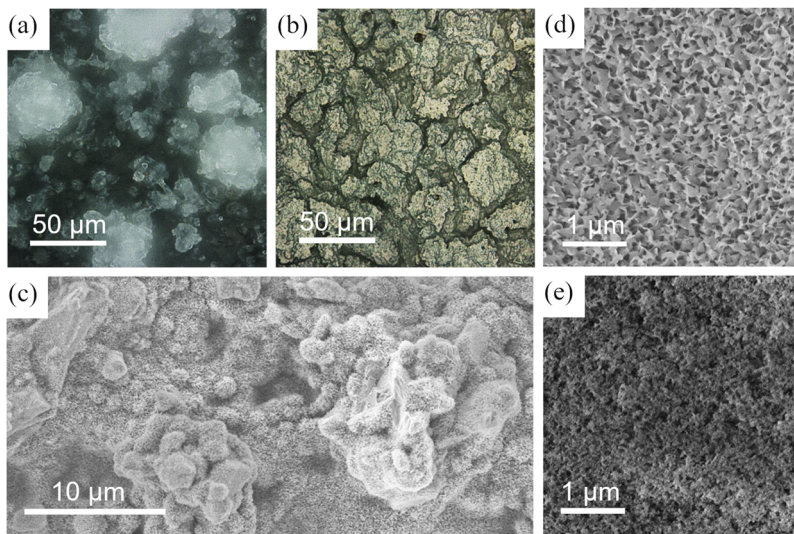


FIG. 1. Depth-composition optical micrographs of (a) acrylic FPOSS spray coating and (b) etched aluminum surface. Scanning electron micrographs of the 80 grit sandblasted, etched, and boehmitized surface, showing (c) hierarchical surface texture before hydrophobization, with roughness features at multiple length scales, (d) boehmite layer showing the characteristic crossed leaflet nanostructure, and (e) hydrophobic silica nanoparticles covering the boehmite texture after treatment with the Glaco solution.

C. Sandblasted, etched, and boehmitized aluminum

It is now well known in the literature that the resistance of a superhydrophobic texture to pressure-induced wetting can be enhanced by incorporating hierarchical roughness features at two or more length scales.⁴¹ Two such surfaces were prepared, each having three tiers of hierarchical roughness produced by first sandblasting (large features of the order of 100 μm), then acid etching (secondary features having sizes of 1 μm –10 μm), and finally boehmitizing in deionized water (tertiary features in the range of 10 nm–100 nm). Two identical aluminum 6061-T6 substrates were first sandblasted with abrasive grits of two different mesh sizes; 80 grit alumina (having an average particle size of 165 μm) was used for the first substrate, and 150 grit alumina (having an average particle size of 89 μm) was used for the other. Both surfaces were then etched in 12M hydrochloric acid for 25 s and boehmitized in boiling water for 30 min. The textured surfaces were hydrophobized by treating them with a commercial water-repellent solution (Glaco Mirror Coat Zero, SOFT99 Corp., Japan) consisting of 30 nm–50 nm size hydrophobic silica particles dispersed in isopropyl alcohol.⁴² A uniform layer of the Glaco solution was sprayed on each surface and allowed to dry in air for 5 min, followed by baking at 250 $^{\circ}\text{C}$ for 30 min; the spraying and baking steps were repeated thrice to obtain robust and uniform coverage. Figures 1(d) and 1(e), respectively, show SEM images of the sandblasted, etched, and boehmitized surface before and after treatment with the Glaco solution; the porous boehmite layer helps retain the silica nanoparticles firmly in the texture and is seen to be fully covered by nanoparticles after three rounds of coating and baking.

III. EXPERIMENTAL METHODS

A. Surface profilometry

Two-dimensional height profiles for all four surfaces were measured using a laser scanning confocal microscope (Keyence VK-X250, Keyence Corporation). A 50 \times objective lens with a numerical aperture of 0.95 was used for all measurements, giving a lateral

spatial resolution of 280 nm and a vertical (height) resolution of 100 nm. The raw height data, acquired from a total scan area of 0.062 mm^2 , consisted of discrete height values $z(x, y)$ on a rectangular grid of 1024 \times 768 scan lines. After minor filtering to remove speckling and noise artifacts and corrections for surface tilt, the raw data were used to obtain the zero-centered height profile $h(x, y) = z(x, y) - \langle z(x, y) \rangle$, where $\langle \dots \rangle$ denotes spatial averaging over the sample area. Figure 2 shows the measured height profiles of all four surfaces; in Fig. 2(d), the data for the 150 grit sandblasted, etched, and boehmitized surface are plotted as a height distribution histogram. The discrete height data were then used to estimate the following statistical measures of roughness:

$$\text{RMS roughness: } w = \sqrt{\langle h^2(x, y) \rangle}, \quad (2)$$

$$\text{RMS slope: } s = \sqrt{\langle |\nabla h(x, y)|^2 \rangle}, \quad (3)$$

$$\text{Wenzel roughness: } r_w = \langle \sqrt{1 + |\nabla h(x, y)|^2} \rangle. \quad (4)$$

It may be apposite to note here that the value of r_w as obtained above, by simple numerical integration of the discrete height data, is dependent on the spatial resolution of measurements; indeed, for a truly self-affine fractal surface with roughness features at all wavelengths, the area average in Eq. (4) would diverge.⁴³ The finite resolution of the profilometer, however, introduces an artificial cutoff on the range of measurable wavelengths, and roughness features smaller than the scan line spacing ($\delta_x = 280$ nm in this case) are inevitably excluded from the measured height profile. This absence of high frequency roughness components limits the usefulness of the value of r_w calculated from discrete data; we employ it only for qualitative comparisons of wetting behavior between surfaces, noting that the numerical value may not be sufficiently accurate to be used directly in surface free energy calculations.

Finally, to obtain a measure of the lateral separation of surface features, we calculated the two dimensional autocorrelation function

$$R(u, v) = w^{-2} \langle h(x+u, y+v) h(x, y) \rangle, \quad (5)$$

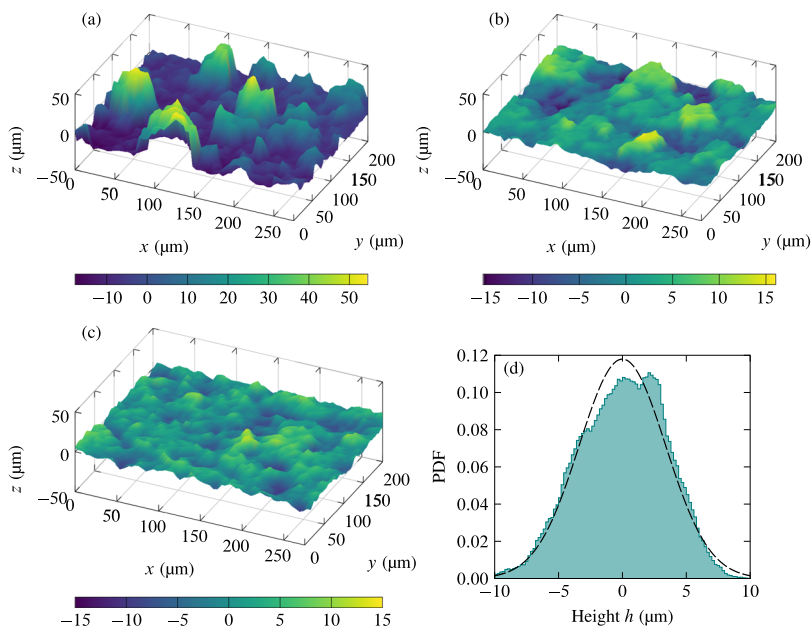


FIG. 2. Two-dimensional surface profilograms of (a) acrylic FPOSS spray coating, (b) etched aluminum, and (c) 80 grit sandblasted, etched, and boehmitized surface. Surface heights $h(x, y)$ have been shifted to have zero mean and downsampled for rendering. (d) Height distribution histogram for the 150 grit sandblasted, etched, and boehmitized surface. The dashed curve is the probability distribution function (PDF) for a Gaussian surface with the same mean square roughness ($w = 3.36 \mu\text{m}$).

where u and v are the spatial lags in the x and y directions, respectively. The mean autocorrelation length λ was then obtained as the radial lag r at which $\hat{R}(r, \theta) = R(r \cos \theta, r \sin \theta)$ decays to the value $1/e$, averaged over all directions θ along the surface (details are included in the [supplementary material](#)). The values of w , s , r_w , and λ were calculated at two or three different spots on each surface and then averaged; the final values are reported in [Table I](#).

B. Contact angle measurements

The advancing and receding contact angles on all four surfaces were measured with a contact angle goniometer (Model 590, Ramé-hart Instrument Co.) using the drop volume method. Drops of deionized water were dispensed through a 22 gauge stainless steel needle, and the drop volume was varied between $10 \mu\text{l}$ and $20 \mu\text{l}$ at a gradual rate of $0.25 \mu\text{l s}^{-1}$; these volumes correspond to excess Laplace pressures of approximately 87 Pa–109 Pa within the drop. The apparent angle at the contact line was estimated during the advancing and receding phases by fitting a circular arc to

the drop profile. Measurements were made at two or three different spots on each surface, and the averaged values are again reported in [Table I](#).

C. Skin friction measurements in turbulent flow

Skin friction measurements were performed on all four superhydrophobic surfaces using a bespoke Taylor-Couette apparatus operating in the featureless turbulent regime⁴⁴ at Reynolds numbers between 1.6×10^4 and 8.9×10^4 , corresponding to wall shear stresses ranging from 2 Pa to 50 Pa. The TC apparatus was coupled to a commercial controlled-stress rheometer (AR-G2, TA Instruments) for accurate speed and torque measurements. [Figure 3](#) shows a sectional view of the bespoke TC test fixture and its main components. The hollow rotating inner cylinder (labeled “rotor” in [Fig. 3](#)) has length $L = 76.2 \text{ mm}$ and radius $R_i = 38.1 \text{ mm}$ and is coupled directly to the spindle of the rheometer, enabling the precise measurement of angular speed Ω and frictional torque \mathcal{T} during experiments. The rotor has a hollow interior which serves as an air-filled

TABLE I. Experimentally measured surface statistics and apparent contact angles for all four rough SH surfaces. The reported errors are the standard deviations of measurements performed at multiple spots on each surface.

Parameter	Acrylic FPOSS spray coating		Sandblasted, etched, and boehmitized aluminum	
		Etched aluminum	80 grit	150 grit
Root mean square roughness, w (μm)	11.0 ± 3.9	6.51 ± 1.91	3.85 ± 0.28	3.36 ± 0.03
Root mean square slope, s	4.54 ± 0.72	2.96 ± 0.89	2.35 ± 0.07	2.95 ± 0.17
Wenzel roughness, r_w	3.24 ± 0.36	2.33 ± 0.32	2.28 ± 0.06	2.70 ± 0.11
Mean autocorrelation length, λ (μm)	15.2 ± 5.2	20.4 ± 4.4	12.3 ± 1.1	7.78 ± 0.48
Advancing contact angle, θ_a (deg)	159 ± 1	162 ± 1	152 ± 1	151 ± 1
Receding contact angle, θ_r (deg)	157 ± 1	158 ± 1	148 ± 1	148 ± 1

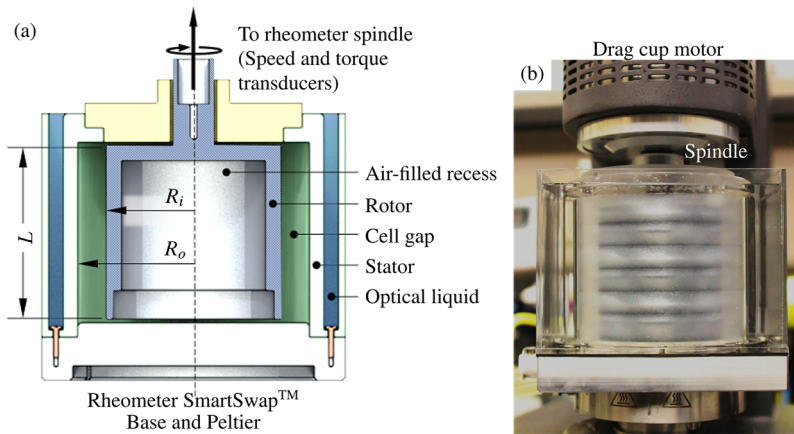


FIG. 3. (a) Schematic diagram of the bespoke Taylor-Couette (TC) apparatus used for experimental skin friction measurements. The labeled dimensions denote the rotor radius $R_i = 38.1$ mm, stator radius $R_o = 50.8$ mm, and rotor length $L = 76.2$ mm. (b) The TC fixture coupled to the AR-G2 rheometer. Three pairs of Taylor vortices are visible through the transparent stator at low Reynolds numbers (here $Re = 156$) on filling the cell gap with a suitable rheoscopic fluid.

recess when submerged, minimizing the rotational moment of inertia and eliminating frictional torque which would otherwise act on the bottom face. The stationary outer cylinder (or “stator”) enclosing the rotor is made of transparent acrylic for visual access to the surface during experiments and has a radius of $R_o = 50.8$ mm. This yields an overall radius ratio of $\eta = R_i/R_o = 0.75$ and an aspect ratio of $\zeta = L/(R_o - R_i) = 6.0$ for the TC apparatus.

Flow measurements on all surfaces were performed at a temperature of (24.4 ± 0.7) °C, using deionized water as the working fluid. For each experiment, the water was first allowed to reach air saturation at the test temperature to prevent depletion of the plastron by diffusion of gas into water. Five similar rotors of the same dimensions—one each for the four superhydrophobic textures and a final smooth rotor for the no-slip baseline—were machined out of aluminum 6061-T6 alloy. Each SH texture was applied to the outer surface of a rotor and then fully submerged in water inside the TC cell gap. Care was taken to ensure that a uniform, reflective plastron was visible on the test surface at the start of each experiment. The fluid-filled space above the rotor serves to completely isolate the plastron from ambient air during measurements and ensures a robust liquid seal that prevents air ingress into the cell at high rotational speeds.

The baseline friction curve for the TC apparatus was obtained using a plain, untextured aluminum rotor with the outer surface polished to a mirror finish (average roughness $R_a = 0.05$ μm and RMS roughness $R_q = 0.07$ μm) to prevent effects of hydrodynamic roughness at even the highest Reynolds numbers achieved experimentally. The time-averaged wall shear stress τ_w at the steady state and the coefficient of friction C_f were then calculated from the torque vs speed data using the expressions

$$\tau_w = \frac{\mathcal{T}}{2\pi R_i^2 L} \quad \text{and} \quad C_f = \frac{2\tau_w}{\rho(R_i\Omega)^2}, \quad (6)$$

where ρ is the density of the working fluid (water). In all tests, the speed Ω of the rotor was increased in discrete steps, and the steady state torque \mathcal{T} was measured after all initial transients had died down and the instantaneous torque values had stabilized to within below 2%. As per the usual convention for Taylor-Couette flows, we define the Reynolds number $Re = R_i\Omega(R_o - R_i)/\nu$ based on the cell gap, ν here being the kinematic viscosity of water. To identify the point

of transition to shear-driven turbulent flow, we followed Lathrop *et al.*⁴⁴ and computed the torque exponent α given by

$$\alpha = \frac{d \ln G}{d \ln Re}, \quad (7)$$

where $G = \mathcal{T}/\rho\nu^2L$ is the nondimensional rotor torque. A plot of the torque exponent α as a function of Re displayed a change of slope at $Re_c \approx 11\,000$, indicating a transition to shear-driven turbulent flow⁴⁴ (more details on the determination of this turbulence transition are included in the [supplementary material](#)). Subsequent measurements on superhydrophobic surfaces were performed at Reynolds numbers above $Re \geq 15\,000$, well into the turbulent flow regime.

Assuming no-slip boundary conditions at the rotor and stator walls, Panton⁴⁵ showed through the method of matched asymptotics that the coefficient of friction in turbulent Taylor-Couette flow must obey a logarithmic friction law of the form

$$\sqrt{\frac{2}{C_f}} = M \ln Re_\tau + N, \quad (8)$$

where $Re_\tau = Re(C_f/2)^{1/2}$ is the shear Reynolds number and M and N are constants that depend on the radius ratio η of the TC geometry. We verified the conformance of our baseline measurements to this logarithmic law by plotting the baseline curve (for $Re > Re_c$) in Prandtl-von Kármán coordinates, as seen in [Figs. 4](#) and [5](#). A least-squares fit of the baseline data (black circles) to Eq. (8) yielded the values $M = 4.52$ and $N = -8.29$ for our particular TC apparatus.

With a superhydrophobic texture (such as those shown in [Figs. 1](#) and [2](#)) applied to the rotor surface, the solid-to-liquid contact is replaced over a large fraction of the wall area by liquid-air interfaces bridging the texture asperities. These regions act almost as shear-free boundaries, allowing the local flow to slip relative to the wall. The usual no-slip condition, however, still holds at the texture asperities, where the underlying solid is in direct contact with the liquid. Srinivasan *et al.*⁸ showed that the overall effect of this composite boundary condition on the outer flow can be modeled as arising from an equivalent “effective” spatially averaged slip length b_{eff} imposed at the rough SH wall. They further derived a modified friction law, analogous to Eq. (8), for the case of a rough SH texture

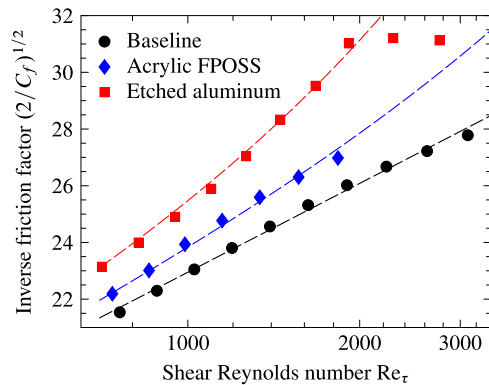


FIG. 4. Experimentally measured skin friction curves for the acrylic FPOSS spray coating and the etched aluminum surface, plotted in Prandtl-von Kármán coordinates. The black dashed line is the baseline friction curve for the Taylor-Couette fixture, given by Eq. (8). The blue and red dashed curves are least-squares fits of Eq. (10) to data points prior to flow-induced plastron failure for the two surfaces.

applied to the inner wall of the TC apparatus

$$\sqrt{\frac{2}{C_f}} = M \ln Re_\tau + N + b_{\text{eff}}^+ \tag{9}$$

where $b_{\text{eff}}^+ = b_{\text{eff}}/\delta_v$. Here b_{eff} is the “effective” slip length on the SH texture and the viscous length δ_v characterizing the turbulent flow is given by $\delta_v = \sqrt{\rho v^2/\tau_w}$. Whereas b_{eff}^+ increases with the Reynolds number,⁸ earlier measurements⁸ and computations^{24,46} have shown that the dimensional effective slip length $b_{\text{eff}} = \delta_v b_{\text{eff}}^+ = (R_o - R_i) b_{\text{eff}}^+ / Re_\tau$ remains almost independent of the Reynolds number for a given SH texture, at least for the range of flow parameters investigated in our study (see the [supplementary material](#) for details). We use the value of the effective slip length b_{eff} , estimated from flow measurements, as the characteristic textural parameter quantifying the drag-reducing ability of our prototype SH surfaces under turbulent flow conditions.

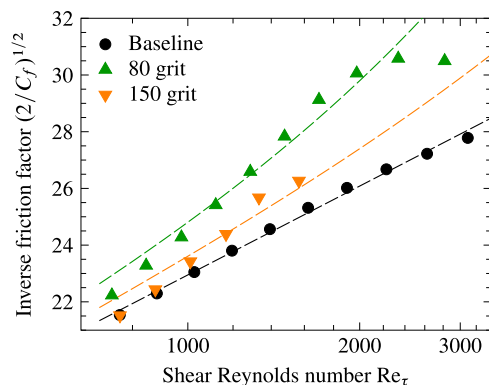


FIG. 5. Skin friction curves for 80 grit and 150 grit sandblasted, etched, and boehmitized surfaces, plotted in Prandtl-von Kármán coordinates. The black dashed line is the baseline friction curve for the Taylor-Couette fixture, given by Eq. (8). The green and orange dashed curves are least-squares fits of Eq. (10) to data points prior to flow-induced plastron collapse.

Substituting $b_{\text{eff}}^+ = b_{\text{eff}} Re_\tau / (R_o - R_i)$ in Eq. (9) and using the values of M and N for the present TC apparatus obtained from the baseline calibration with a smooth rotor, we obtain

$$\sqrt{\frac{2}{C_f}} = 4.52 \ln Re_\tau - 8.29 + \frac{b_{\text{eff}}}{R_o - R_i} Re_\tau. \tag{10}$$

A plot of the skin friction coefficient vs the shear Reynolds number is therefore no longer linear in Prandtl-von Kármán coordinates due to the last term on the right hand side of Eq. (10). The best-fit value of b_{eff} for each SH texture can then be determined using a single-parameter least-squares fit of Eq. (10) to the experimental data; representative curves are shown in Figs. 4 and 5, where the experimentally measured skin friction and the corresponding theoretical fits for the four superhydrophobic surfaces are plotted in Prandtl-von Kármán coordinates. For each surface, a single constant value of an effective slip length b_{eff} characterizes the friction-reducing performance of the texture up until the point of plastron collapse at a critical shear Reynolds number. We can also directly evaluate, for each surface, a percentage drag reduction (DR) as the percentage decrease in wall shear stress produced by the superhydrophobic texture vis-à-vis a smooth, no-slip boundary at the same Reynolds number

$$DR = \frac{\tau_w^0 - \tau_w}{\tau_w^0} \times 100\%. \tag{11}$$

Here, τ_w^0 is the baseline shear stress measured on the smooth, untextured rotor at the same Reynolds number Re (or, equivalently, the same rotor speed Ω). The percentage DR as a function of the Reynolds number Re for the four surfaces is shown in Fig. 6. The percentage DR initially increases with the increase in Reynolds number, which is consistent with the results of previous experimental and computational studies in the literature.^{8,21,23} However, a flow-induced wetting transition and partial loss of the plastron layer eventually occur at high Reynolds numbers, with a concomitant loss of drag-reducing ability of the texture. Indeed, Fig. 6 shows that the percentage DR on all four surfaces initially increases with Re , reaches a maximum, and subsequently decreases due to progressive loss of the trapped air from within the texture. The loss of the plastron at high Reynolds numbers was also confirmed visually by observing the

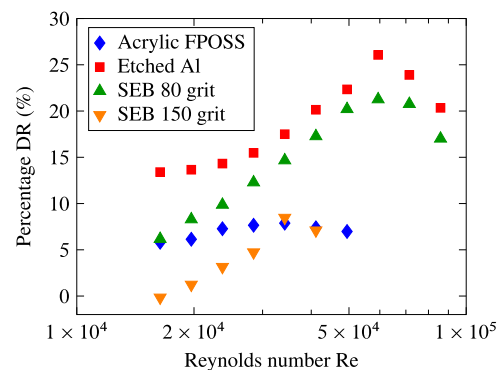


FIG. 6. Percentage reduction in skin friction (in comparison to a smooth, untextured rotor) as a function of the Reynolds number for all four superhydrophobic surfaces. The abbreviation “SEB” denotes sandblasted, etched, and boehmitized aluminum.

rotor surface through the transparent stator during flow tests; the depletion of the plastron layer resulted in a decrease in the reflectivity and luster of the texture when observed underwater. The divergence of the experimental data from the theoretical curves in Figs. 4 and 5 marks the onset of this wetting transition, and this also corresponds to the point of maximum DR for each surface, as seen in Fig. 6. We thus define a critical or “failure” shear stress τ_f as the magnitude of the wall shear stress τ_w at which this occurs and use this parameter to compare the robustness of the four scalable surface textures under turbulent flow conditions.

IV. RESULTS AND DISCUSSION

Figure 7 summarizes the results of our drag reduction measurements and compares the performance of the four superhydrophobic textures in terms of the maximum percentage DR obtained, the effective slip length b_{eff} of the texture in turbulent flow [determined by fitting the data in Figs. 4 and 5 to Eq. (10)], and the wall shear stress at which plastron failure on the superhydrophobic surface is observed. Of the four surfaces tested in the TC apparatus, the largest effective slip length and the greatest percentage drag reduction were obtained in the case of the etched aluminum surface. The 80 grit sandblasted, etched, and boehmitized surface was the most resistant to plastron collapse under turbulent flow conditions, withstanding a maximum wall shear stress of 26.9 Pa. The 80 grit surface also gave a much higher slip length than the 150 grit surface, suggesting that the length scale of the primary roughness has a significant influence on the drag-reducing ability in the case of hierarchical superhydrophobic textures. The surface easiest to fabricate was the

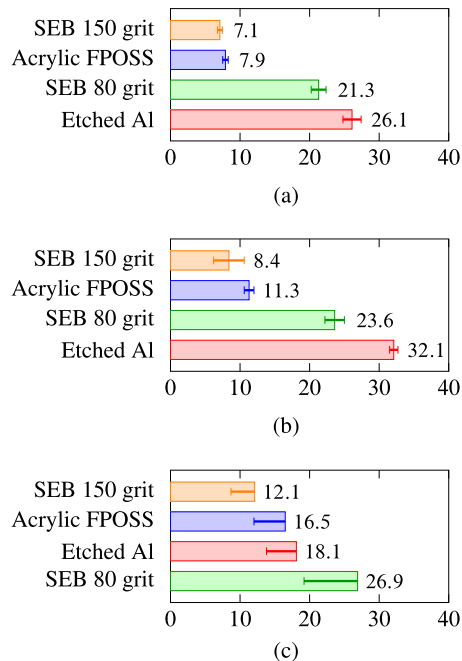


FIG. 7. Superhydrophobic textures ranked in the order of increasing (a) maximum percentage drag reduction, (b) effective slip length, and (c) wall shear stress at plastron collapse. “SEB” stands for sandblasted, etched, and boehmitized aluminum.

acrylic FPOSS spray-on coating; however, it was also mechanically fragile, and subsequent to the loss of the plastron layer at large Re , it suffered irreversible mechanical degradation after a single test run inside the TC fixture. The adhesion of the polymer matrix to the underlying smooth metal surface of the rotor was also observed to be rather poor. All four surfaces eventually failed by plastron loss during flow tests, well before the maximum shear stress attainable in the TC apparatus ($\tau_{w,\text{max}} = 50$ Pa) was reached. However, after removal of the rotor from the TC cell and drying in air, the superhydrophobicity of the test surfaces, with the exception of the acrylic FPOSS spray-on coating, was restored. Subsequent reimmersion in the TC cell resulted in a new plastron layer, and a repeat experiment could be performed.

In Fig. 8, the effective slip lengths for the four surfaces are plotted against various statistical measures of surface roughness listed in Table I, namely, the root mean square roughness w , the root mean square slope s , the Wenzel roughness r_w , and the mean autocorrelation length λ . The three textured aluminum surfaces have comparable values of RMS roughness ($3.4 \mu\text{m} \leq w \leq 6.5 \mu\text{m}$) but display a large spread in values of the effective slip length b_{eff} . The acrylic FPOSS spray-coated surface, on the other hand, has a very large roughness value ($w = 11.0 \mu\text{m}$), nearly twice that of the aluminum surfaces, and consequently yields only a modest value of effective slip length, comparable to (and slightly larger than) the 150 grit sandblasted, etched, and boehmitized surface. The decline in drag-reducing ability at large values of surface roughness is consistent with previously reported results in the literature.^{36,47–49} The liquid-air interface established on a submerged, rough SH texture forms a complex undulating surface of constant mean curvature,³⁵ the Young-Laplace equation is satisfied locally at every point on this meniscus, and the equilibrium contact angle is maintained at the three phase contact line established at the solid-liquid-air interface. Past studies of the effects of interface deformation on drag reduction have shown that the slip length is the largest when the interface is perfectly flat and decreases with increasing deformation of the interface, either into or out of the flow region.^{48,49} Inasmuch as the RMS roughness w dictates the scale of vertical fluctuations in surface height, the value of w must be sufficiently small to ensure that the air-water interface, which forms the flow boundary, remains largely flat.

It is evident from the data shown in Fig. 8 that the drag-reducing ability of these scalable, randomly rough textures in turbulent flow does not correlate simply with any single measure of the surface roughness. We therefore considered in more detail how these different measures characterizing the surface texture interact with the characteristic length scale of the turbulent flow. Bidkar *et al.*³⁶ have reported turbulent drag measurements on rough superhydrophobic surfaces with various roughness values, obtained using a water tunnel at large Reynolds numbers of $1 \times 10^6 \leq Re \leq 9 \times 10^6$. They observed that an appreciable reduction in drag was obtained only on surfaces with roughness at least an order of magnitude smaller than the thickness of the viscous sublayer, which extends to a distance of about $5\delta_v$ from the wall. Consequently, they proposed $w^+ = w/\delta_v \leq 0.5$ as a necessary condition to achieve superhydrophobic drag reduction in turbulent boundary layer flow. Similar conclusions were also arrived at by Gose *et al.* in their recent study.³⁷ At large values of roughness, tall surface asperities projecting through the liquid-air interface may interact with the

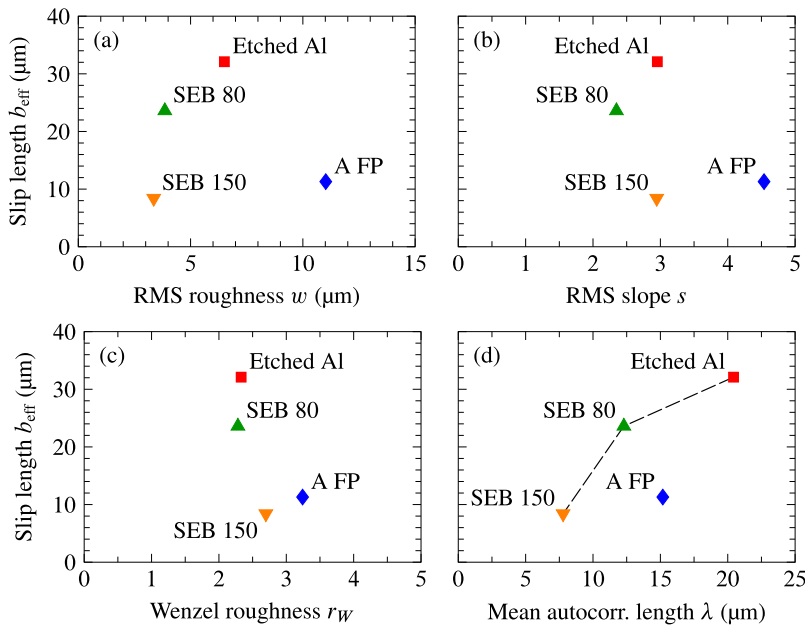


FIG. 8. The effective slip length b_{eff} plotted against (a) RMS roughness, (b) RMS slope, (c) Wenzel roughness and (d) the mean autocorrelation length, for the four randomly rough superhydrophobic surfaces. The dashed lines in panel (d) are only for visual reference. The error bars for b_{eff} values are comparable to or smaller than the size of the data markers and have been omitted for clarity; the numerical error values are included in the [supplementary material](#). Abbreviations: “A FP”—acrylic FPOSS spray coating, “Etched Al”—etched aluminum, “SEB 80”—80 grit sandblasted, etched, and boehmitized aluminum, and “SEB 150”—150 grit sandblasted, etched, and boehmitized aluminum.

viscous sublayer, obstructing the flow path and incurring additional form drag, thereby offsetting the drag reduction generated by interfacial slip. The roughness criterion becomes more restrictive at high Reynolds numbers when the thickness of the viscous sublayer decreases and becomes of the order of a few micrometers or lower. A sufficiently large amplitude superhydrophobic texture may then simply act as hydrodynamic roughness, producing zero drag reduction or even a net drag increase. In [Fig. 9\(a\)](#), we plot the root mean

square roughness w^+ expressed in wall units for all four SH textures, calculated at the failure shear stress τ_f . Whereas the scaled roughness is less than unity for the three aluminum textures, the acrylic FPOSS spray-coating displays a large value of $w^+ \approx 1.6$, which explains the relatively small value of b_{eff} obtained for this texture in spite of its excellent water repellency in air and also its rapid mechanical deterioration after the onset of flow-induced wetting that is observed during tests.

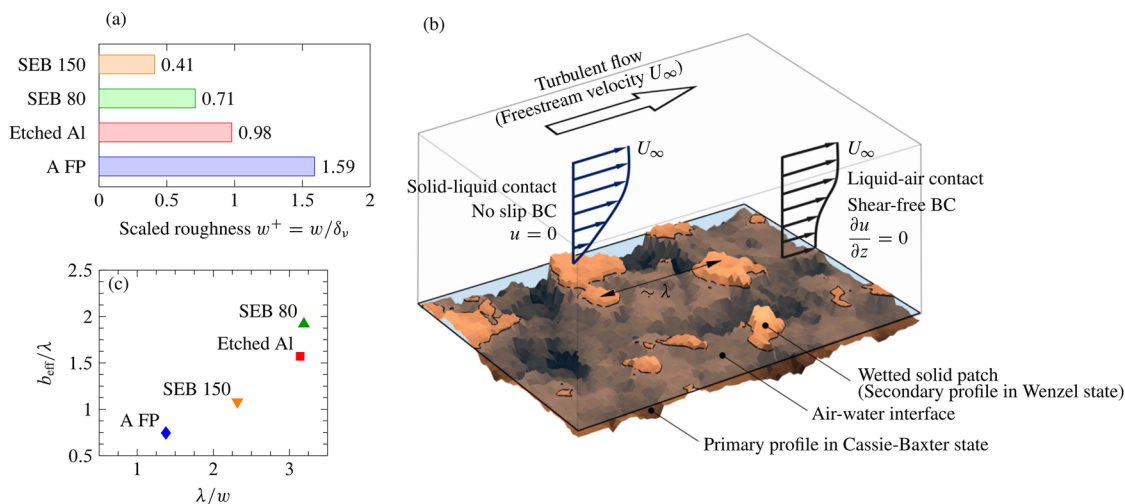


FIG. 9. (a) The root mean square roughness expressed in wall units for all four SH textures at the point of failure. (b) Schematic representation of a submerged, randomly rough, multiscale SH texture in turbulent flow. The flat interface depicted here is only for illustration; the actual air-water interface would be curved and may not all be at the same level. (c) The ratio b_{eff}/λ as a function of the ratio of surface length scales λ/w for the four SH textures; b_{eff} increases with increasing λ and decreasing w . Abbreviations used are identical to those in [Fig. 8](#).

Excluding the data point for the acrylic FPOSS surface, whose poor performance can be attributed to its large surface roughness, we notice from Fig. 8 a strong dependence of the slip length b on the mean autocorrelation length λ of the texture. For fractal self-affine surfaces, the autocorrelation length represents the only characteristic lateral length scale of the texture and is representative of the length scale between individual surface asperities;⁴³ in this respect, it is analogous to the spatial periodicity L for regularly patterned surfaces consisting of ridges or posts.⁵⁰ This strong dependence of the effective slip length on the mean autocorrelation length is therefore in qualitative agreement with the known theoretical results for regularly patterned surfaces. For instance, over a regular 2D array of posts with spatial periodicity L , the slip length scales according to $b \sim L/\sqrt{\phi}$ in the limit $\text{Re} \rightarrow 0$ and as $b \sim L^{1/3} \delta_v^{2/3} / \sqrt{\phi}$ in the limit of turbulent flow at high Re , where ϕ is the areal fraction of the solid substrate in direct contact with the liquid phase.^{19,24} In either case, we observe that the expected dimensional slip length b increases with the spacing L between posts. Figure 8(d) supports the conclusion that provided the surface roughness remains sufficiently small, the relevant textural parameter (analogous to L for periodic textures) to be optimized in the design of drag-reducing randomly rough SH textures is the lateral autocorrelation length λ .

Examining Fig. 8, no direct correlation is evident between the effective slip length b_{eff} and either the surface slope s or the Wenzel roughness r_W ; surfaces with comparable values of surface slope or Wenzel roughness are seen to have widely different values of b_{eff} . We therefore conclude, within confidence bounds imposed by the limited number of data points, that the effective slip length on a rough superhydrophobic texture is not strongly dependent on either parameter. A large Wenzel roughness, however, is known to be an important requirement for ensuring the stability of the air-water interface on the surface, without which turbulent pressure fluctuations will quickly trigger a transition to the Wenzel state, resulting in drag increase.^{32,35} Bottiglione and Carbone³⁵ performed numerical simulations of wetting and interface penetration on one-dimensional, randomly generated, self-affine fractal profiles; their results show that the mean square surface slope s^2 is a key determinant of the breakthrough pressure p_W , i.e., the externally imposed excess pressure in the liquid phase at which a catastrophic wetting transition to the Wenzel state is triggered. For 2D isotropic Gaussian surfaces, they further showed that the root mean square slope and the Wenzel roughness are interrelated approximately as $r_W \approx \sqrt{\pi} s/2$. A sufficiently large Wenzel roughness r_W , or equivalently a large root mean square slope s , is therefore required to ensure that a transition to the Wenzel state does not occur even under the intense pressure fluctuations encountered in turbulent flow. A large r_W also serves to restrict the extent of penetration of the interface into the texture so that hydrodynamic roughness effects and the associated drag increase are minimized. Using a free energy analysis, they also derived a simple design rule for robust superhydrophobicity under externally imposed pressure, given by

$$r_W > -\frac{1}{\cos \theta_Y}, \tag{12}$$

where θ_Y is the Young (or equilibrium) contact angle on the solid substrate. Since $\cos \theta_Y < 0$ for a hydrophobic surface, the above

criterion yields a lower bound for the Wenzel roughness r_W of the texture and by extension a corresponding lower bound on the root mean square surface slope s .

A sufficiently large mean square slope therefore appears necessary to stabilize the liquid-air interface against failure. Concurrently, we also require a large autocorrelation length to obtain a large effective slip length and appreciable drag-reducing ability for the texture. For a Gaussian self-affine surface, it may be shown that the surface roughness w , the surface slope s , and the autocorrelation length λ scale as $w \sim s\lambda$;^{43,51,52} therefore, a large value of λ in conjunction with a large value of s would unavoidably entail a large value of w , which conflicts with the requirement of small surface roughness. For self-affine textures, therefore, the requirements for interface stability (large s) and low hydrodynamic roughness (small w) appear contradictory—one may be improved only at the expense of the other. However, this inference rests on the assumption that the surface is self-affine with a uniform scaling behavior from the smallest to the largest length scales; a possible workaround is thus the incorporation of hierarchical roughness at two or more successively finer length scales into the texture. For a self-affine profile, the slope s_k of the individual roughness components scales as $s_k^2 \sim k^{(1-2H)}$, where k is the spatial (angular) wavenumber and H is the roughness exponent, or the Hurst exponent, of the fractal profile.^{35,43} Most real surfaces generated by random texturing processes have a Hurst exponent $H > 0.5$, typically in the range $0.7 < H < 1$; thus, the slope of various spectral components of roughness decreases with increasing k (i.e., with decreasing wavelength).⁵³ The solid-liquid contact on a randomly rough SH texture is therefore a combination of localized Cassie and Wenzel regimes, with the liquid bridging over the large-scale primary roughness asperities, but fully wetting the small-scale secondary roughness atop those asperities,³⁵ which we schematically depict in Fig. 9(b). If we now ignore the fully wetted secondary features, the “effective” contact angle θ_e at the contact line as it traverses the contour of the primary roughness profile is given approximately by the Wenzel equation⁹

$$\cos \theta_e = r'_W \cos \theta_Y. \tag{13}$$

Here, r'_W is the Wenzel roughness of the secondary texture superimposed on the primary profile. Equation (12) then becomes less restrictive on the Wenzel roughness of the primary profile r_W

$$r_W > -\frac{1}{\cos \theta_e} = -\frac{1}{r'_W \cos \theta_Y}. \tag{14}$$

The primary roughness profile can now have a smaller mean square slope and consequently a smaller mean square roughness for a given lateral spacing between surface features. The effective slip length b_{eff} is determined by the spacing of peaks in the primary profile since it depends only on the extent of the free interface available between the successive contact patches at which the local fluid flow must necessarily come to rest. We may thus anticipate that the addition of a secondary roughness would have minimal influence on the effective slip length or the drag-reducing ability of the overall surface. Hierarchical texturing, which is already a well-known technique in the literature, thus permits us to design superhydrophobic textures having a small roughness and a large interasperity spacing, without sacrificing the stability of the liquid-air interface under turbulent flow conditions.

In conclusion, we arrive at the following key considerations for designing scalable, randomly rough superhydrophobic textures for turbulent drag reduction applications: (a) the texturing process must be optimized to generate a large mean autocorrelation length ($\lambda/\delta_v \gg 1$) for the primary roughness profile, (b) the texture should possess a sufficiently small roughness ($w^+ < 1$) to mitigate roughness-induced increases in the hydrodynamic drag, and (c) the texture should ideally incorporate secondary (and possibly higher order) hierarchical roughness features to ensure the stability of the air-water interface against turbulent fluctuations. The simultaneous influence of the lateral and vertical length scales on the effective slip length of the texture can be seen in Fig. 9(c), which shows the nondimensional slip length b_{eff}/λ for the four surfaces plotted against the ratio of texture length scales, λ/w . The effective slip length b_{eff} increases systematically as the mean autocorrelation length λ is increased and decreases when the RMS roughness w is increased, supporting statements (a) and (b) above.

V. CONCLUSION

In this paper, we evaluated the drag reduction performance of four prototype superhydrophobic surfaces in turbulent flow, using a combination of flow tests, surface profilometry, and contact angle measurements. Each surface had a randomly rough surface texture, generated by means of scalable mechanical and chemical texturing processes—spray coating, sandblasting, chemical etching, and boehmitization. Submerged flow tests were performed on the surfaces in the featureless turbulent flow regime inside a custom-built Taylor-Couette apparatus, at Reynolds numbers between 1.64×10^4 and 8.59×10^4 , and an effective slip length was determined for each surface from frictional torque measurements. Drag reductions of up to 26% were measured under turbulent flow conditions. The key textural parameter determining the effective slip length and drag-reducing ability of randomly rough superhydrophobic textures was the mean autocorrelation length λ , which quantifies the lateral separation of surface asperities; this is analogous to the influence of the spatial periodicity L on the slip length b in the case of regularly patterned SH surfaces. As seen in Fig. 9(c), the presence of large lateral spacing between roughness peaks, in conjunction with a small root mean square roughness (compared to the viscous length scale δ_v of the turbulent boundary layer), and, additionally, the presence of hierarchical roughness features were identified as three critical requirements for the successful design of scalable, randomly rough superhydrophobic textures intended for turbulent drag reduction applications.

An important practical consideration not addressed in this study is the longevity of the plastron on a submerged superhydrophobic texture, which would be of primary concern in real-life applications where sustained drag reduction performance is required over long durations of time. Even the best designed superhydrophobic surface will fail if the air trapped in the texture is depleted; this may occur either due to shear-induced drainage³² or by forced convective mass transfer in the turbulent boundary layer.⁵⁴ Several strategies have been explored in the literature to sustain drag reduction through active replenishment of the gas layer, such as supplying pressurized gas to the texture through a porous backing plate,⁵⁵ vapor generation by Leidenfrost heating,^{56–58} as well as electrochemical^{59,60} or catalyst-mediated gas generation.⁶¹ The

feasibility and efficacy of these methods on scalable SH textures have to be investigated in high Reynolds number flows similar to those typically encountered in real-life service.

SUPPLEMENTARY MATERIAL

See [supplementary material](#) for details on the calculation of the mean autocorrelation length and other textural statistics from the 2D surface height profile, determination of the point of transition from turbulent Taylor vortices (TTV) to the featureless turbulent flow regime inside the TC apparatus, and estimation of the effective slip length from skin friction measurements in turbulent TC flow.

ACKNOWLEDGMENTS

Financial support for this work was provided by the Office of Naval Research (ONR) under the Multidisciplinary University Research Initiatives (MURI) program through contract number 3002453814.

REFERENCES

- M. Perlin and S. L. Ceccio, *Mitigation of Hydrodynamic Resistance: Methods to Reduce Hydrodynamic Drag* (World Scientific Publishing Co., 2014).
- S. A. Mäkiharju, M. Perlin, and S. L. Ceccio, "On the energy economics of air lubrication drag reduction," *Int. J. Archit. Ocean Eng.* **4**, 412 (2012).
- S. L. Ceccio, "Friction drag reduction of external flows with bubble and gas injection," *Annu. Rev. Fluid Mech.* **42**, 183 (2010).
- E. S. Winkel, G. F. Oweis, S. A. Vanapalli, D. R. Dowling, M. Perlin, M. J. Solomon, and S. L. Ceccio, "High Reynolds number turbulent boundary layer friction drag reduction from wall-injected polymer solutions," *J. Fluid Mech.* **621**, 259 (2009).
- K. A. Lay, R. Yakushiji, S. Mäkiharju, M. Perlin, and S. L. Ceccio, "Partial cavity drag reduction at high Reynolds numbers," *J. Ship Res.* **54**, 109 (2010); available at <https://www.ingentaconnect.com/content/snname/jsr/2010/00000054/00000002/art00003>.
- B. Dean and B. Bhushan, "Shark-skin surfaces for fluid-drag reduction in turbulent flow: A review," *Philos. Trans. R. Soc., A* **368**, 4775 (2010).
- K. B. Golovin, J. W. Gose, M. Perlin, S. L. Ceccio, and A. Tuteja, "Bioinspired surfaces for turbulent drag reduction," *Philos. Trans. R. Soc., A* **374**, 20160189 (2016).
- S. Srinivasan, J. A. Kleingartner, J. B. Gilbert, R. E. Cohen, A. J. B. Milne, and G. H. McKinley, "Sustainable drag reduction in turbulent Taylor-Couette flows by depositing sprayable superhydrophobic surfaces," *Phys. Rev. Lett.* **114**, 014501 (2015).
- D. Quéré, "Wetting and roughness," *Annu. Rev. Mater. Res.* **38**, 71 (2008).
- N. J. Shirtcliffe, G. McHale, M. I. Newton, C. C. Perry, and F. B. Pyatt, "Plastron properties of a superhydrophobic surface," *Appl. Phys. Lett.* **89**, 104106 (2006).
- J. P. Rothstein, "Slip on superhydrophobic surfaces," *Annu. Rev. Fluid Mech.* **42**, 89 (2010).
- J. Davenport, R. N. Hughes, M. Shorten, and P. S. Larsen, "Drag reduction by air release promotes fast ascent in jumping emperor penguins—A novel hypothesis," *Mar. Ecol.: Prog. Ser.* **430**, 171 (2011).
- C.-L.-M.-H. Navier, "Mémoire sur les lois du mouvement des fluides," *Mem. Acad. Sci. Inst. Fr.* **6**, 389 (1827).
- J. R. Philip, "Flows satisfying mixed no-slip and no-shear conditions," *Z. Angew. Math. Phys.* **23**, 353 (1972).
- J. R. Philip, "Integral properties of flows satisfying mixed no-slip and no-shear conditions," *Z. Angew. Math. Phys.* **23**, 960 (1972).
- E. Lauga and H. A. Stone, "Effective slip in pressure driven Stokes flow," *J. Fluid Mech.* **489**, 55 (2003).
- C. Cottin-Bizonne, C. Barentin, E. Charlaix, L. Bocquet, and J.-L. Barrat, "Dynamics of simple liquids at heterogeneous surfaces: Molecular dynamics simulations and hydrodynamic description," *Eur. Phys. J. E* **15**, 427 (2004).

- ¹⁸C. Schönecker, T. Baier, and S. Hardt, "Influence of the enclosed fluid on the flow over a microstructured surface in the Cassie state," *J. Fluid Mech.* **740**, 168 (2014).
- ¹⁹C. Ybert, C. Barentin, C. Cottin-Bizonne, P. Joseph, and L. Bocquet, "Achieving large slip with superhydrophobic surfaces: Scaling laws for generic geometries," *Phys. Fluids* **19**, 123601 (2007).
- ²⁰J. Seo, R. Garcia-Mayoral, and A. Mani, "Pressure fluctuations and interfacial robustness in turbulent flows over superhydrophobic surfaces," *J. Fluid Mech.* **783**, 448 (2015).
- ²¹T. Min and J. Kim, "Effects of hydrophobic surface on skin-friction drag," *Phys. Fluids* **16**, L55 (2004).
- ²²M. B. Martell, J. B. Perot, and J. P. Rothstein, "Direct numerical simulations of turbulent flows over superhydrophobic surfaces," *J. Fluid Mech.* **620**, 31 (2009).
- ²³M. B. Martell, J. P. Rothstein, and J. B. Perot, "An analysis of superhydrophobic turbulent drag reduction mechanisms using direct numerical simulation," *Phys. Fluids* **22**, 065102 (2010).
- ²⁴J. Seo and A. Mani, "On the scaling of the slip velocity in turbulent flows over superhydrophobic surfaces," *Phys. Fluids* **28**, 025110 (2016).
- ²⁵R. J. Daniello, N. E. Waterhouse, and J. P. Rothstein, "Drag reduction in turbulent flows over superhydrophobic surfaces," *Phys. Fluids* **21**, 085103 (2009).
- ²⁶H. Park, G. Sun, and C.-J. Kim, "Superhydrophobic turbulent drag reduction as a function of surface grating parameters," *J. Fluid Mech.* **747**, 722 (2014).
- ²⁷B. J. Rosenberg, T. Van Buren, M. K. Fu, and A. J. Smits, "Turbulent drag reduction over air- and liquid-impregnated surfaces," *Phys. Fluids* **28**, 015103 (2016).
- ²⁸M. A. Samaha, H. V. Tafreshi, and M. Gad-el-Hak, "Effects of hydrostatic pressure on the drag reduction of submerged aerogel-particle coatings," *Colloids Surf., A* **399**, 62 (2012).
- ²⁹K. Moaven, M. Rad, and M. Taeibi-Rahni, "Experimental investigation of viscous drag reduction of superhydrophobic nano-coating in laminar and turbulent flows," *Exp. Therm. Fluid Sci.* **51**, 239 (2013).
- ³⁰X. J. Feng and L. Jiang, "Design and creation of superwetting/antiwetting surfaces," *Adv. Mater.* **18**, 3063 (2006).
- ³¹M. Nosonovsky and B. Bhushan, "Superhydrophobic surfaces and emerging applications: Non-adhesion, energy, green engineering," *Curr. Opin. Colloid Interface Sci.* **14**, 270 (2009).
- ³²E. Aljallis, M. A. Sarshar, R. Datla, V. Sikka, A. Jones, and C.-H. Choi, "Experimental study of skin friction drag reduction on superhydrophobic flat plates in high Reynolds number boundary layer flow," *Phys. Fluids* **25**, 025103 (2013).
- ³³J. Zhang, H. Tian, Z. Yao, P. Hao, and N. Jiang, "Mechanisms of drag reduction of superhydrophobic surfaces in turbulent boundary layer flow," *Exp. Fluids* **56**, 179 (2015).
- ³⁴B. V. Hokmabad and S. Ghaemi, "Turbulent flow over wetted and non-wetted superhydrophobic counterparts with random structure," *Phys. Fluids* **28**, 015112 (2016).
- ³⁵F. Bottiglione and G. Carbone, "Role of statistical properties of randomly rough surfaces in controlling superhydrophobicity," *Langmuir* **29**, 599 (2013).
- ³⁶R. A. Bidkar, L. Leblanc, A. J. Kulkarni, V. Bahadur, S. L. Ceccio, and M. Perlin, "Skin friction drag reduction in the turbulent regime using random-textured hydrophobic surfaces," *Phys. Fluids* **26**, 085108 (2014).
- ³⁷J. W. Gose, K. Golovin, M. Boban, J. M. Mabry, A. Tuteja, M. Perlin, and S. L. Ceccio, "Characterization of superhydrophobic surfaces for drag reduction in turbulent flow," *J. Fluid Mech.* **845**, 560 (2018).
- ³⁸P. Kim, M. J. Kreder, J. Alvarenga, and J. Aizenberg, "Hierarchical or not? Effect of the length scale and hierarchy of the surface roughness on omniphobicity of lubricant-infused substrates," *Nano Lett.* **13**, 1793 (2013).
- ³⁹S. Srinivasan, S. S. Chhatre, J. M. Mabry, R. E. Cohen, and G. H. McKinley, "Solution spraying of poly(methyl methacrylate) blends to fabricate microtextured, superoleophobic surfaces," *Polymer* **52**, 3209 (2011).
- ⁴⁰J. Yang, Z. Zhang, X. Xu, X. Men, X. Zhu, and X. Zhou, "Superoleophobic textured aluminum surfaces," *New J. Chem.* **35**, 2422 (2011).
- ⁴¹M. Nosonovsky, "Multiscale roughness and stability of superhydrophobic biomimetic interfaces," *Langmuir* **23**, 3157 (2007).
- ⁴²C. Lv, P. Hao, Z. Yao, and F. Niu, "Departure of condensation droplets on superhydrophobic surfaces," *Langmuir* **31**, 2414 (2015).
- ⁴³M. Pelliccione and T.-M. Lu, *Evolution of Thin Film Morphology* (Springer, 2008).
- ⁴⁴D. P. Lathrop, J. Fineberg, and H. L. Swinney, "Transition to shear-driven turbulence in Couette-Taylor flow," *Phys. Rev. A* **46**, 6390 (1992).
- ⁴⁵R. L. Panton, "Scaling laws for the angular momentum of a completely turbulent Couette flow," *C. R. Acad. Sci. Paris, Ser. II* **315**, 1467 (1992).
- ⁴⁶C. T. Fairhall, N. Abderrahaman-Elena, and R. Garcia-Mayoral, "The effect of slip and surface texture on turbulence over superhydrophobic surfaces," *J. Fluid Mech.* **861**, 88 (2019).
- ⁴⁷S. Richardson, "On the no-slip boundary condition," *J. Fluid Mech.* **59**, 707 (1973).
- ⁴⁸M. Sbragaglia and A. Prosperetti, "A note on the effective slip properties for microchannel flows with ultrahydrophobic surfaces," *Phys. Fluids* **19**, 043603 (2007).
- ⁴⁹A. Steinberger, C. Cottin-Bizonne, P. Kleimann, and E. Charlaix, "High friction on a bubble mattress," *Nat. Mater.* **6**, 665–668 (2007).
- ⁵⁰This is strictly true only in the case of self-affine surfaces, with a uniform fractal scaling behavior at all length scales. "Mounded" surfaces, on the other hand, have an underlying characteristic wavelength λ' introduced during the texturing process, with a corresponding peak in the PSD spectrum. For such surfaces, the wavelength λ' is more representative of the lateral spacing of asperities or "mounds," whereas the autocorrelation length λ gives the lateral size of these mounds.⁴³ The roughness spectra of each of the four surfaces in this case showed no single dominant wavelength and more closely resembled a self-affine behavior.
- ⁵¹M. S. Longuet-Higgins, "Statistical properties of an isotropic random surface," *Philos. Trans. R. Soc., A* **250**, 157 (1957).
- ⁵²P. R. Nayak, "Random process model of rough surfaces," *J. Lubr. Technol.* **93**, 398 (1971).
- ⁵³B. N. J. Persson, "On the fractal dimension of rough surfaces," *Tribol. Lett.* **54**, 99 (2014).
- ⁵⁴M. A. Samaha, H. V. Tafreshi, and M. Gad-el-Hak, "Influence of flow on longevity of superhydrophobic coatings," *Langmuir* **28**, 9759 (2012).
- ⁵⁵H. Ling, S. Srinivasan, K. Golovin, G. H. McKinley, A. Tuteja, and J. Katz, "High-resolution velocity measurements in the inner part of turbulent boundary layers over super-hydrophobic surfaces," *J. Fluid Mech.* **801**, 670 (2016).
- ⁵⁶I. U. Vakarelski, N. A. Patankar, J. O. Marston, D. Y. Chan, and S. T. Thoroddsen, "Stabilization of Leidenfrost vapour layer by textured superhydrophobic surfaces," *Nature* **489**, 274 (2012).
- ⁵⁷I. U. Vakarelski, D. Y. Chan, and S. T. Thoroddsen, "Leidenfrost vapour layer moderation of the drag crisis and trajectories of superhydrophobic and superhydrophilic spheres falling in water," *Soft Matter* **10**, 5662 (2014).
- ⁵⁸D. Saranadhi, D. Chen, J. A. Kleingartner, S. Srinivasan, R. E. Cohen, and G. H. McKinley, "Sustained drag reduction in a turbulent flow using a low-temperature Leidenfrost surface," *Sci. Adv.* **2**, e1600686 (2016).
- ⁵⁹C. Lee and C. J. Kim, "Underwater restoration and retention of gases on superhydrophobic surfaces for drag reduction," *Phys. Rev. Lett.* **106**, 014502 (2011).
- ⁶⁰M. Xu, G. Sun, and C. J. Kim, "Infinite lifetime of underwater superhydrophobic states," *Phys. Rev. Lett.* **113**, 136103 (2014).
- ⁶¹D. Panchanathan, A. Rajappan, K. K. Varanasi, and G. H. McKinley, "Plastron regeneration on submerged superhydrophobic surfaces using *in situ* gas generation by chemical reaction," *ACS Appl. Mater. Interfaces* **10**, 33684 (2018).